HHS Public Access

Author manuscript

Science. Author manuscript; available in PMC 2017 November 17.

Published in final edited form as:

Science. 2013 April 19; 340(6130): 337–341. doi:10.1126/science.1231391.

Multicompartment Mesoporous Silica Nanoparticles with Branched Shapes: An Epitaxial Growth Mechanism

Teeraporn Suteewong[1,2,*], **Hiroaki Sai**[1,*], **Robert Hovden**[3], **David Muller**[3,4], **Michelle S. Bradbury**[2], **Sol M. Gruner**[4,5,6], and **Ulrich Wiesner**[1,†]

[1]Department of Materials Science and Engineering, Cornell University, Ithaca, NY 14853, USA

[2]Department of Radiology, Memorial Sloan-Kettering Cancer Center, 1275 York Avenue, New York, NY 10065, USA

[3]School of Applied and Engineering Physics, Cornell University, Ithaca, NY 14853, USA

[4]Kavli Institute at Cornell for Nanoscale Science, Ithaca, NY 14853, USA

[5]Department of Physics, Cornell University, Ithaca, NY 14853, USA

[6]Cornell High Energy Synchrotron Source (CHESS), Cornell University, Ithaca, NY 14853, USA

Abstract

Mesoporous nanomaterials have attracted widespread interest because of their structural versatility for applications including catalysis, separation, and nanomedicine. We report a one-pot synthesis method for a class of mesoporous silica nanoparticles (MSNs) containing both cubic and hexagonally structured compartments within one particle. These multicompartment MSNs (mc-MSNs) consist of a core with cage-like cubic mesoporous morphology and up to four branches with hexagonally packed cylindrical mesopores epitaxially growing out of the cubic core vertices. The extent of cylindrical mesostructure growth can be controlled via a single additive in the synthesis. Results suggest a path toward high levels of architectural complexity in locally amorphous, mesostructured nanoparticles, which could enable tuning of different pore environments of the same particle for specific chemistries in catalysis or drug delivery.

Mesoporous silica materials have attracted widespread interest because of their versatility in pore structure, surface chemistry, and macroscopic form (particles, coatings, or bulk materials) (1, 2). A variety of mesostructures have been explored, including hexagonal, cage-like cubic, cubic bicontinuous, and platelet ordered structures as well as, most recently, dodecagonal quasicrystalline structures (3, 4). Mesoporous silica nanoparticles (MSNs) are of particular interest owing to their large surface area and pore volume, the ability to functionalize their outer and/or inner surfaces, and the tunability of their pore geometry (5, 6). Multicompartment nanoparticles have been developed from self-assembling designer

†Corresponding author: ubw1@cornell.edu.
*These authors contributed equally to this work.

Supplementary Materials www.sciencemag.org/cgi/content/full/340/6130/337/DC1
Materials and Methods
Figs. S1 to S4
Reference (28)

macromolecules (7–9). Such materials have been compared with cells as the paradigm for a multicompartment system, in which different units (e.g., nucleus or organelles) have different well-defined functions. In potential drug delivery applications for these materials, each compartment could be tuned to carry different and incompatible components (7).

Despite the existing library of geometrical variations of the silica pore mesostructure, the synthesis of analogous multicompartment MSNs (mc-MSNs) remains a challenge, partly because of the lack of growth mechanisms enabling pore structure control in different compartments of the same particle. Identifying such growth mechanisms would enable access to locally amorphous, mesoscopically ordered nanoparticles with a high degree of architectural complexity yet highly controlled shapes and assemblies.

The field of solution-grown semiconductor nanoparticle synthesis provides a possible clue to the creation of such architectures. Such nanoparticles may have polymorphic atomic structures that are epitaxially attached at the interface from a core, leading to branched inorganic nanostructures with well-defined and characteristic shapes such as tetrapods and dendrimers (10–12). Rather than epitaxy from atomic structures, mesostructural epitaxy exists in mesoporous silica—that is, for various cubic lattices as well as between $Pm\bar{3}n$ and two-dimensional (2D) hexagonal lattices (13–18). We investigated how such mesostructural epitaxy can be used in low molar mass surfactant coassembly to generate mc-MSNs with branched shapes in which the branches exhibit pore geometries different from that of the core, based on different mesostructural lattices.

Highly aminated cubic MSNs with cage-like pore structure consistent with $Pm\bar{3}n$ symmetry were synthesized at room temperature from mixed organosilane precursors via a one-pot, hexadecyltrimethylammonium bromide (CTAB) surfactant–directed sol-gel synthesis, with variations in ethyl acetate concentration [EtOAc] (19–21). When [EtOAc] was increased, mesoporous silica branches with hexagonal cylinder pore structure grew from specific facets of the cubic MSN cores (Fig. 1, A and B). Bright-field transmission electron microscopy (BF-TEM) images indicated that these two parts or “compartments” of the nano-particles have a well-defined structural relation when viewed along the [110] zone axis (Fig. 1A). Furthermore, some particles possessed multiple branches (Fig. 1B). High-angle annular dark-field scanning TEM (HAADF-STEM) images of mc-MSNs along the [100] zone axis (Fig. 1C) showed the characteristic four-fold internal structure consistent with the faceted overall particle shape. Fast Fourier transform (FFT) patterns of the HAADF-STEM image exhibited spots for the (110), (200), and (210) planes, consistent with $Pm\bar{3}n$ symmetry (Fig. 1D). Closer inspection of the particle in Fig. 1C revealed the corresponding characteristic four-fold internal patterns (Fig. 1E). Figure 1F depicts the corresponding model schematic viewed from a similar angle as in Fig. 1C. Although the size of micellar pores relative to the overall particle is modified in this model to better show the internal structure, the external shape of the particle in Fig. 1C is consistent with the model in Fig. 1F, where the cube is truncated at its corners with (111) planes and its sides with (110) planes. Occasionally the branches were also observed to be faceted along the $(10\bar{1}0)$ planes (fig. S1), coincident with (110) planes on the core, which provided a basis for determining the facets in the model. When HAADF-STEM images were obtained along the [110] zone axis (Fig. 1G) of the core, the internal linear pore structure of the branch was clearly observed. Figure 1H shows a

magnified image of the connecting region between the core and the branch. Red lines representing the cylindrical pores of the branch are in registry with the micellar pores of the core depicted as red dots, visually supporting an epitaxial relationship between the mesostructures of the two compartments.

FFT of the core region showed spots corresponding to the $Pm\bar{3}n$ peak positions with the (110) zone axis (Fig. 1I), whereas FFT of the connected region showed an overlap of sharp (211) spots from the cubic lattice and diffuse (10) spots from the 2D hexagonal lattice, also consistent with an epitaxial relationship between the two structures (Fig. 1J). This epitaxial relationship can be modeled by a sphere-to-rod transition of micelles, as illustrated in Fig. 1, K to M. A $Pm\bar{3}n$ cage-like cubic structure can be composed of a body-centered cubic arrangement of micelles plus pairs of micelles on each cubic face (Fig. 1K). Sectioning the unit cell at the (111) plane, each blue micelle resides on top of a set of three yellow micelles, making a locally layered order (Fig. 1L). Figure 1M is a top-view schematic showing where the 2D hexagonal channels are placed with respect to the (111) cubic planes; the hexagonal lattice of the blue micelles is in registry with the hexagonally ordered channels, consistent with the observations shown in Fig. 1H and highlighted by the red lines and dots.

The relative amount of hexagonal versus cubic mesostructure could be controlled by increasing [EtOAc] in the initial mixture (Fig. 2). Low-magnification TEM images of MSNs synthesized from 91, 274, and 457 mM EtOAc (Fig. 2, A, D, and G, respectively) show hexagonally ordered branches only at elevated concentrations (Fig. 2A shows only cubic MSNs). The length of these hexagonally ordered branches increased with increasing [EtOAc] (compare Fig. 2, D and G). Most of the mc-MSNs synthesized from 274 mM EtOAc had short branches with diameters equal to or smaller than the core size (Fig. 2D). In the sample synthesized from 457 mM EtOAc, these branches grew to rods as long as 2 μm, often in a nonstraight fashion (Fig. 2G). Higher-magnification images show that the nanoparticles synthesized from 274 mM EtOAc (Fig. 2E) consist of a branch attached to a core with cage-like cubic structure. At 457 mM EtOAc (Fig. 2H), for most of the rods we could not find a core portion, suggesting structural transformation from cubic to hexagonal mesostructure.

Small-angle x-ray scattering (SAXS) patterns (Fig. 2, C, F, and I) of these samples averaging over macroscopic material volumes corroborate the local TEM observations, in that the relative intensities of the peaks consistent with $P6mm$ 2D hexagonal symmetry increased at the expense of those consistent with $Pm\bar{3}n$ symmetry. The cubic MSN sample synthesized from 91 mM EtOAc showed reflections consistent with $Pm\bar{3}n$ symmetry and a unit cell size of 9.65 nm (Fig. 2C) (19). At 274 mM EtOAc, reflections consistent with 2D hexagonal symmetry and a unit cell size of 4.80 nm were superposed with reflections consistent with $Pm\bar{3}n$ symmetry and a unit cell size of 10.5 nm (Fig. 2F). The (211) reflection for the cubic lattice coincided closely with the (10) reflection for the hexagonal lattice, with lattice mismatch of ~3%, corroborating an epitaxial relation between the two lattices. The pore-to-pore spacings for the hexagonal branches in the mc-MSNs synthesized from 274 mM EtOAc were 8% larger than those for purely hexagonal MSNs synthesized in the absence of (3-aminopropyl)triethoxysilane (APTES) and were 3 to 4% larger than those synthesized in the presence of varying amounts of APTES (fig. S2) (20, 22). On the other hand, the (211)

spacing of the cubic core was 4.95 nm, indicating that the 2D hexagonal lattice is stretched to accommodate for the lattice mismatch. At 457 mM EtOAc, reflections consistent with $Pm\bar{3}n$ had almost disappeared, leaving mostly those consistent with 2D hexagonal symmetry and a pore-to-pore spacing of 4.86 nm (Fig. 2I). The increase in spacing as a function of [EtOAc] for both cubic and hexagonal structures (fig. S2) is likely associated with swelling of the hydrophobic micelle cores with EtOAc molecules.

To establish a structure-property relationship for these mc-MSNs, we performed nitrogen sorption measurements (Fig. 3). All three samples showed characteristic type IV isotherms, with the capillary condensation of mesopores occurring at nitrogen partial pressure around 0.3. The mc-MSNs containing more hexagonal pores (i.e., synthesized from higher [EtOAc]) exhibited a sharper mesopore condensation behavior, as reflected in the pore size distribution calculated using nonlocal density functional theory (NLDFT) (Fig. 3, inset). The cubic MSN showed a broad distribution of pore sizes centered at 3.6 nm and extending up to 4.5 nm; mc-MSNs with increasing numbers of hexagonal pores exhibited narrower pore size distributions centered around 3 to 4 nm. This sorption behavior is consistent with the cage-like pore geometry with constricted windows between the cages in the cubic core and the straight channel geometry in the hexagonal branches (23).

The above trend in MSN structure as a function of [EtOAc] sheds light on a possible growth mechanism of hexagonal branches emanating from the cubic cores. In basic conditions, EtOAc is known to hydrolyze over time into ethanol and acetic acid, which quenches an equimolar amount of base and thus lowers the pH of the reaction mixture (24). At room temperature, the kinetic constant of ester hydrolysis is 5.4 liters mol^{-1} min^{-1} (25). Increasing [EtOAc] from 91 mM to 457 mM while keeping the concentration of base (ammonium hydroxide and APTES) constant at ~200 mM imposes two effects on the solution pH (fig. S3). First, it induces an increase in the hydrolysis rate and thus in the rate of pH drop. Second, it lowers the final pH of the solution asymptotically with respect to [EtOAc], because the hydrolysis reaction slows as the hydroxide ions are quenched. As pH decreases below the negative logarithm of the acid dissociation constant (pK_a) of APTES, the predominant state of the amine group of APTES becomes positively charged, which repels against the charged head groups of the structure-directing CTAB cations. This change in the charge state of APTES may induce a structural change in the CTAB micelles. Although at high pH some of the uncharged APTES molecules can intercalate between CTAB head groups, charge repulsion prevents this swelling at lower pH. The resulting change in micelle curvature has been suggested as the main factor driving a morphological change from cage-like cubic to hexagonal, in agreement with the observed transition from a cubic core to hexagonal branches growing off of this core in the present study (23, 26). The room-temperature synthesis protocol used here enables fine-tuning of the sol-gel kinetics against pH change, providing control over the mc-MSN morphology. In energy-dispersive spectroscopy–derived elemental maps, we did not observe substantial variations in the amine content for the cubic versus hexagonal parts of the nanoparticles (fig. S4), suggesting high inclusion of APTES in both cubic and hexagonal pore walls.

Nucleation of hexagonally mesostructured compartments on the cubic MSN cores can occur on multiple facets of the cubic core, most evident at intermediate [EtOAc]. At 137 mM and

183 mM EtOAc, although most particles still showed only one branch per core, a fraction had one, two, three, and even four branches (Fig. 4, A and B). Close TEM examination of these mc-MSNs revealed that the angles at which the hexagonally structured branches grew were in agreement with models in which hexagonal branches grow in ⟨111⟩ directions off of the core, consistent with the epitaxial relationship (compare TEM images with corresponding models in Fig. 4, C to F and H to K, respectively). No MSN with more than four branches was observed in our samples, although we did observe some mc-MSNs in which hexagonal branches that grew in two distinct directions merged into one branch with a large diameter (compare TEM image with model in Fig. 4, G and L). On a truncated cubic structure, there are eight (111) equivalent surfaces corresponding to the number of cube vertices, giving eight equivalent sites for hexagonal branches to form and grow. As a particular branch grows, it may deplete the available silica in its direct vicinity, thus preventing growth of another branch next to it. This is one possible explanation for why the vast majority of observed branches had grown on non-nearest (111) core surfaces and why the maximum number of branches observed was only four. We further hypothesize that when two nearest neighboring sites nucleate hexagonal branches, geometrical crowding joins the neighboring nuclei as they grow. Such merging and overgrowth of hexagonal rods also reduces the number of rods per particle and increases the rod diameter relative to the core particle size. This may be what leads to the observed structures in the 457 mM EtOAc sample (Fig. 2G).

Finally, to access higher-level architectures, we performed mc-MSN syntheses in a two-step fashion by adding further monomers at different time points of the reaction (21). The TEM results in Fig. 4M, displaying a high number of dimers (two cubes) and trimers (three cubes) connected via bridges, are encouraging. They suggest that further tuning of reaction conditions holds promise for achieving even more complex architectures—for example, through switching back and forth between cubic-to-hexagonal and hexagonal-to-cubic transitions—similar to what has been observed for semiconductor nanoparticles or colloids with valence (11, 27).

Supplementary Material

Refer to Web version on PubMed Central for supplementary material.

Acknowledgments

Supported by NSF single-investigator grant DMR-1104773 and by a Partnership for Research and Education in Materials (PREM) program at Norfolk State University through NSF grant DMR-1205457. We thank L. Estroff, R. Dieckmann, and K. Hur (Cornell University) for discussions on multiple branch growth and K. W. Tan (Cornell University) for assistance with EM. This work made use of the TEM and STEM supported by the Cornell Center for Materials Research with support from the NSF Materials Research Science and Engineering Centers program (DMR-1120296), and CHESS, which is supported by the NSF and the National Institute of General Medical Sciences under NSF award DMR-0936384. T.S. is grateful for a Thai Government Scholarship under the Ministry of Science and Technology.

References and Notes

1. Yanagisawa T, Shimizu T, Kuroda K, Kato C. Bull Chem Soc Jpn. 1990; 63:988.
2. Kresge CT, Leonowicz ME, Roth WJ, Vartuli JC, Beck JS. Nature. 1992; 359:710.

3. Hoffmann F, Cornelius M, Morell J, Fröba M. Angew Chem Int Ed. 2006; 45:3216.
4. Xiao CH, Fujita N, Miyasaka K, Sakamoto Y, Terasaki O. Nature. 2012; 487:349. [PubMed: 22810699]
5. Vallet-Regí M, Balas F, Arcos D. Angew Chem Int Ed. 2007; 46:7548.
6. Slowing II, Vivero-Escoto JL, Wu CW, Lin VS. Adv Drug Deliv Rev. 2008; 60:1278. [PubMed: 18514969]
7. Li ZB, Kesselman E, Talmon Y, Hillmyer MA, Lodge TP. Science. 2004; 306:98. [PubMed: 15459387]
8. Cui HG, Chen ZY, Zhong S, Wooley KL, Pochan DJ. Science. 2007; 317:647. [PubMed: 17673657]
9. Chandrawati R, van Koeverden MP, Lomas H, Caruso F. J Phys Chem Lett. 2011; 2:2639.
10. Manna L, Milliron DJ, Meisel A, Scher EC, Alivisatos AP. Nat Mater. 2003; 2:382. [PubMed: 12764357]
11. Yin Y, Alivisatos AP. Nature. 2005; 437:664. [PubMed: 16193041]
12. Talapin DV, et al. Nano Lett. 2007; 7:2951. [PubMed: 17845068]
13. Srinivasu P, Lim S, Kubota Y, Tatsumi T. Catal Today. 2006; 111:379.
14. Han L, Sakamoto Y, Che S, Terasaki O. Chemistry. 2009; 15:2818. [PubMed: 19191233]
15. Atluri R, Bacsik Z, Hedin N, Garcia-Bennett AE. Micropor Mesopor Mater. 2010; 133:27.
16. Han L, Miyasaka K, Terasaki O, Che SN. J Am Chem Soc. 2011; 133:11524. [PubMed: 21696179]
17. Che SN, Kamiya S, Terasaki O, Tatsumi T. J Am Chem Soc. 2001; 123:12089. [PubMed: 11724619]
18. Kamiya S, Tanaka H, Che S, Tatsumi T, Terasaki O. Solid State Sci. 2003; 5:197.
19. Suteewong T, et al. J Am Chem Soc. 2011; 133:172. [PubMed: 21158438]
20. Suteewong T, et al. Chem Mater. 2012; 24:3895.
21. See supplementary materials on *Science* Online.
22. Suteewong T, et al. J Mater Chem. 2010; 20:7807.
23. Atluri R, Sakamoto Y, Garcia-Bennett AE. Langmuir. 2009; 25:3189. [PubMed: 19437783]
24. Schulz-Ekloff G, Rathousky J, Zukal A. Int J Inorg Mater. 1999; 1:97.
25. Dittert LW, Higuchi T. J Pharm Sci. 1963; 52:852. [PubMed: 14061044]
26. Ogura M, Miyoshi H, Naik SP, Okubo T. J Am Chem Soc. 2004; 126:10937. [PubMed: 15339178]
27. Wang Y, et al. Nature. 2012; 491:51. [PubMed: 23128225]

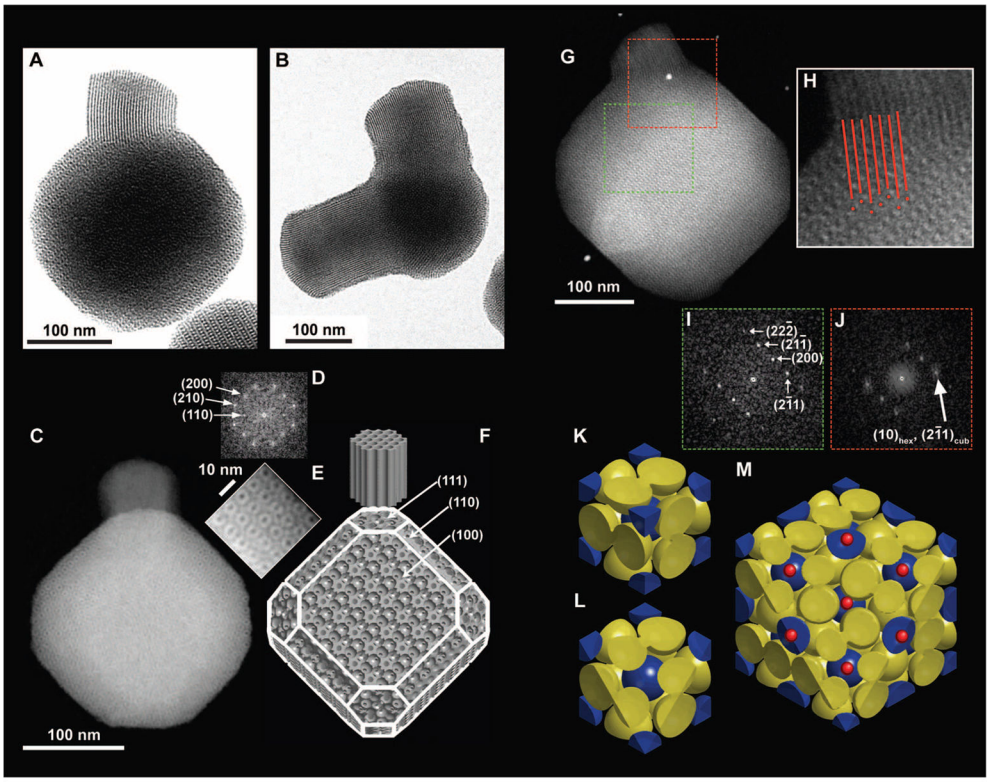

Fig. 1. Geometrical description of mc-MSNs

(**A**) BF-TEM image of a branch with hexagonal pore structure emanating from one corner of a core with cubic pore structure. (**B**) BF-TEM image showing two branches emanating from two corners of the core. (**C**) HAADF-STEM image of (100) projection of the core. (**D**) FFT of the entire cubic core part of the image in (C). (**E**) Magnified image of the top right edge of the particle in (C). (**F**) Schematics of a model mc-MSN. Miller indices for some of the representative facets are provided as a visual guide. (**G**) HAADF-STEM image of a mc-MSN exhibiting the (110) projection of the core. (**H**) Magnified image of the connecting region between the core and branch in (G), with red lines and dots indicating projected vacancy positions to demonstrate the structural registry/epitaxy. (**I**) FFT of the cubic core region in (G) (green box). (**J**) FFT of the connected region in (G) (red box). (**K** to **M**) Model visualization of the epitasial relationship of mesopores at the interface of (111) $Pm\bar{3}n$ cubic and (0001) $P6mm$ hexagonal planes. (K) Unit cell of the $Pm\bar{3}n$ cage-like structure exhibiting body-centered cubic lattice micelles (blue spheres) and pairs of micelles on the faces (yellow spheres). (L) (111) plane cut of a single unit cell. (M) (111) plane cut of a 2 × 2 × 2 lattice, additionally showing the positions of expected hexagonal channels as small red dots.

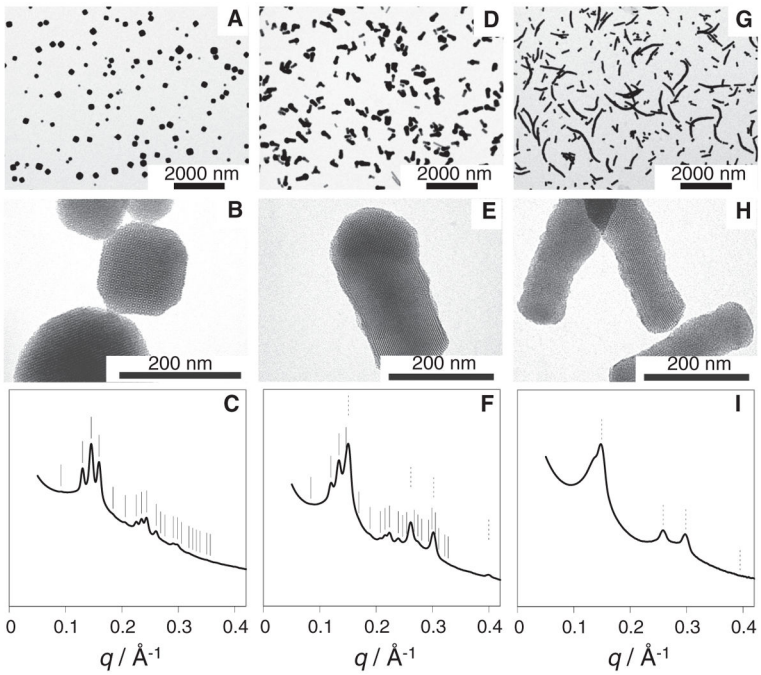

Fig. 2. TEM images and SAXS patterns of aminated MSNs synthesized with varying [EtOAc]

(**A**, **D**, and **G**) Low-magnification TEM images of MSNs prepared from (A) 91 mM, (B) 274 mM, and (C) 457 mM EtOAc. (**B**, **E**, and **H**) Higher-magnification TEM images of the MSNs in (A), (D), and (G). (**C**, **F**, and **I**) The corresponding SAXS patterns (q denotes the scattering vector magnitude, defined as $q = 4\pi \sin\theta/\lambda$, where 2θ is the total scattering angle and λ is the x-ray wavelength). In the SAXS patterns, expected peak positions from cubic and hexagonal lattices are indicated by solid and dotted lines, respectively. Data for 91 mM EtOAc are adapted from (19).

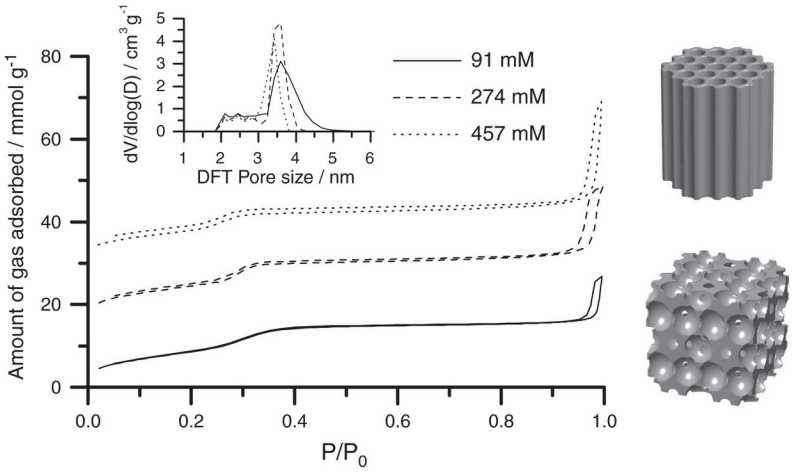

Fig. 3. Nitrogen sorption isotherms of MSNs synthesized with varying [EtOAc]

Isotherms for mc-MSNs prepared from 274 mM and 457 mM EtOAc are offset along the *y* axis by 15 and 30 mmol/g, respectively (P/P_0 denotes the nitrogen partial pressure). The inset shows pore size distributions obtained from NLDFT calculations based on the respective absorption branches. The models on the right provide a direct comparison of the pore structures of hexagonal and cubic lattices.

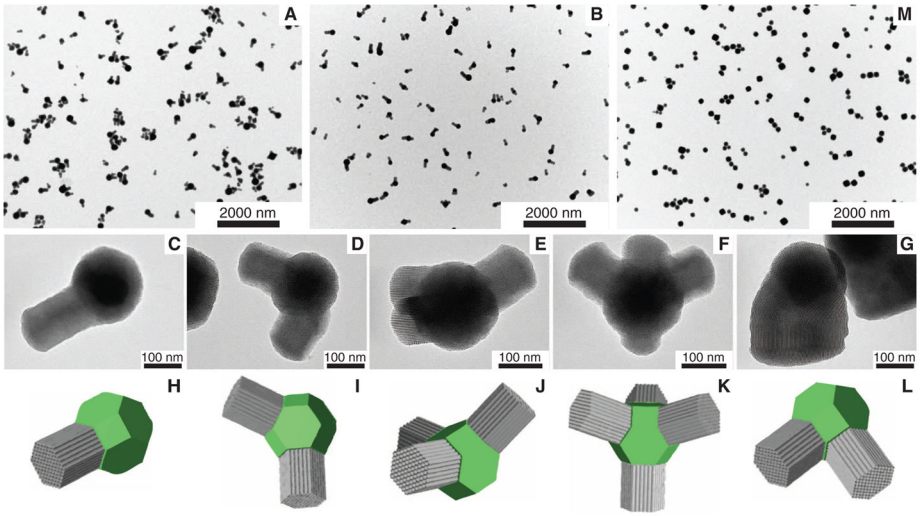

Fig. 4. TEM images and models of mc-MSNs with complex mesostructures

(**A** and **B**) Low-magnification TEM images of mc-MSNs prepared from (A) 137 mM and (B) 183 mM EtOAc. (**C** to **G**) High-magnification TEM images of mc-MSNs in the 183 mM EtOAc batch with (C) one arm, (D) two arms, (E) three arms, (F) four arms, and (G) two arms merged into one. (**H** to **L**) Models corresponding to the images in (C) to (G). Cores are shown as green truncated cubes; branches are represented as gray columns. (**M**) Low-magnification TEM image of mc-MSNs where additional silane precursors (one-half of the initial amount) were injected after 30 min of aging time (21).